RESEARCH ARTICLE

WILEY

Multifluid flows with weak and strong discontinuous interfaces using an elemental enriched space

Sergio R. Idelsohn[1,2,3,4] | Juan M. Gimenez[3,4] | Norberto M. Nigro[3,4]

[1]Institució Catalana de Recerca i Estudis Avançats (ICREA), Barcelona, Spain

[2]Centre Internacional de Mètodes Numèrics en Enginyeria (CIMNE), Barcelona, Spain

[3]Centro de Investigación de Métodos Computacionales (CIMEC-UNL-CONICET), Santa Fe, Argentina

[4]Facultad de Ingeniería y Ciencias Hídricas, Universidad Nacional del Litoral, Santa Fe, Argentina

Correspondence
Sergio R. Idelsohn, Gran Capitan s/n, Edificio C1, Campus Nord UPC, 08034 Barcelona, Spain.
Email: sergio@cimne.upc.edu

Summary

In a previous paper, the authors presented an elemental enriched space to be used in a finite-element framework (EFEM) capable of reproducing kinks and jumps in an unknown function using a fixed mesh in which the jumps and kinks do not coincide with the interelement boundaries. In this previous publication, only scalar transport problems were solved (thermal problems). In the present work, these ideas are generalized to vectorial unknowns, in particular, the incompressible Navier-Stokes equations for multifluid flows presenting internal moving interfaces. The advantage of the EFEM compared with global enrichment is the significant reduction in computing time when the internal interface is moving. In the EFEM, the matrix to be solved at each time step has not only the same amount of degrees of freedom (DOFs) but also the same connectivity between the DOFs. This frozen matrix graph enormously improves the efficiency of the solver. Another characteristic of the elemental enriched space presented here is that it allows a linear variation of the jump, thus improving the convergence rate, compared with other enriched spaces that have a constant variation of the jump. Furthermore, the implementation in any existing finite-element code is extremely easy with the version presented here because the new shape functions are based on the usual finite-element method shape functions for triangles or tetrahedrals, and once the internal DOFs are statically condensed, the resulting elements have exactly the same number of unknowns as the nonenriched finite elements.

KEYWORDS

CFD, discontinuous fields, EFEM, enriched FE spaces, incompressible fluid flows, internal interfaces, multifluids, Navier-Stokes equations

1 | INTRODUCTION

In a previous paper,[1] the authors presented an elemental enriched space capable of reproducing kinks and jumps of the unknown functions using a fixed mesh in which the jumps and kinks do not coincide with the interelement boundaries. In that publication, only thermal problems were solved in which the unknown variable was a scalar function. In this work, we generalize the previous ideas to a vectorial field such as the incompressible Navier-Stokes equations.

Kinks and jumps in the velocity and in the pressure fields are present in many engineering problems, particularly in multifluids and fluid-structure interaction problems. In the case of multifluids (several fluids with different physical

properties), the dynamics of the interface between the fluids involved plays a dominant role. The computation of the interface between various immiscible fluids or the free surfaces is extremely difficult because neither the shape nor the positions of the interfaces are a priori known. The 2 main approaches to solving these problems are as follows: one based on using a moving mesh that follows the discontinuity, named interface-tracking methods, and another based on using a fixed mesh (some times refined in that part of the domain where the interfaces cross during the evaluation), named interface-capturing methods.

In this last method (see other works[2-4]), the interface is determined by an implicit function immersed in a Eulerian (fixed) mesh, and the flow problem is solved considering the fluids as a single effective fluid with variable properties. Popular methods of this type are the volume-of-fluid technique[5-7]; the level-set method,[8-11] which advects the interface using Eulerian strategies; and the Particle Finite-Element Method—Second Generation,[12-15] which employs a Lagrangian method.

Independent of the method used to move the internal interface, the problem in fixed-mesh methods is that the change in physical material properties along the interface introduces kinks or possibly jumps that must be captured in the solution of the global problem in order to have accurate results. Some authors try to fulfill this issue by refining the mesh near the interface without introducing any possibility of having a kink or a jump inside the elements.

For such problems, when the interface does not necessarily conform to the element edges (in 2-dimensional [2D]) or faces (in 3-dimensional [3D]), the finite-element solution, either for continuous or discontinuous approximations across interelement boundaries, suffers from a suboptimal convergence rate. This poor approximation leads to spurious velocities near the interface that may significantly affect the precision and the robustness of numerical simulations (see, eg, the work of Ganesan et al[16]). Furthermore, the need for a local refinement around the interface implies the refinement of the mesh in almost the entire domain where the possible position of the interface may go through when the interface moves.

A number of methods have been developed to overcome these difficulties. One possibility is to add degrees of freedom (DOFs) or to enrich the finite-element space at the elements cut by the interface. Minev et al[17] and, later, Chessa and Belytschko[18] adopted an enrichment technique nowadays called XFEM, a name coined in the context of fracture mechanics, and also named GFEM by other authors.[19] Both approaches lead to optimal orders of convergence, but the main drawback is that the additional DOFs cannot be eliminated before assembly. The XFEM approach has also been used recently in 2-phase flows.[20,21] These kinds of enrichment have been also called global enrichment or nodal enrichment, previously stated XFEM or GFEM. A method that avoids the inclusion of additional DOFs is one that allow to statically condense the additional DOFs prior to the assembly. For this reason, these kinds of enrichment have been named elemental enrichment or EFEM.[22,23] A generalization of the treatment of kinks and jumps in the pressure field was presented by Ausas et al.[24] However, the enriched space proposed in the aforementioned literature[24] works satisfactorily for the pressure field in the Navier-Stokes equations but does not work correctly for the enrichment of the temperature field in a typical thermal problem or for the enrichment of the displacement or the velocity field in solid or fluid mechanics problems. As previously stated, Idelsohn et al[1] presented a new elemental enriched space that allows a better approximation of second-order equations in which an integration by parts is needed. The generalization of these ideas to the incompressible Navier-Stokes equations is presented next.

As presented by Oliver et al[23] and Sánchez et al[25] in the context of fracture simulations, the computational cost of XFEM is always larger than that of the corresponding EFEM due to the stiffness matrix construction and the solver (in turn, the most time-consuming operations), mainly in 3D problems. The difference, they showed, is due to the elemental condensing done in EFEM, where additional DOFs do not substantially contribute to the computational costs, irrespective of their number. That conclusion can be extended to internal interface problems and leads to a significant reduction in computing time when the internal interface is moving. If this kind of problem is simulated with EFEM, then the matrix to be solved at each time step has not only the same amount of DOFs but also the same connectivity between the DOFs. This means that the matrix graph (profile) remains constant, whereas in the XFEM, the matrix graph is permanently changing.

The advantage of not modifying the matrix can be exploited by employing both direct and iterative solvers for sparse linear equation systems. The former is used by an important community seduced by the independence from matrix conditioning and the goodness when parallelized solution techniques, as additive Schwartz, are employed. Here, if the matrix graph does not change during simulation, a unique prefactorized matrix can be used to solve that system at each time step, thus reducing substantially the global central processing unit time. In the case of using iterative solvers, Oliver et al[23] report in its fig. 25 that the central processing unit time differences increase (up to 3 times in 3D) when the ratio between the number of enriched and nonenriched elements, ie, the proportion of the interface along the domain, grows. Moreover, the cost of matrix assembly should be considered only once with EFEM (just the coefficients must be updated),

thus avoiding the costly continuous reassembling of the system matrix done by XFEM where memory chunk allocation is permanently required for each time step.

The disadvantage of the EFEM is the impossibility of exact consistency with the internal continuities required for the variational form. How to mitigate these inconsistencies for the case of multifluids (also called variational crimes) is one of the main targets of this work. Another characteristic of the elemental enriched space presented here is that it allows a linear variation of the jump, improving the convergence rate to the exact solution, compared with other enriched spaces that have a constant variation of the jump. The implementation in any existing finite-element code is extremely easy in both 2 and 3 spatial dimensions. This is because the new shape functions are based on the usual finite-element method shape functions for triangles or tetrahedrals, and once the internal DOFs are statically condensed, the resulting elements have exactly the same number of unknowns as the nonenriched finite elements. To show the accuracy of the new space proposed, simple but very convincing examples of the solution of the Navier-Stokes equations for single-phase and multifluid flows using a fixed background mesh are presented as numerical examples.

2 | THE GOVERNING EQUATIONS

2.1 | Conservation of linear momentum

The momentum conservation in the entire domain reads:

$$\rho \frac{D\mathbf{u}}{Dt} = \nabla \cdot \boldsymbol{\sigma} + \mathbf{b}, \tag{1}$$

where ρ is the density, $\mathbf{u}$ is the velocity vector, $\boldsymbol{\sigma}$ is the stress tensor, $\mathbf{b}$ is a source vector, and $\frac{D\mathbf{u}}{Dt}$, the material derivative, is the acceleration vector that can be also written in a Eulerian frame as $\frac{D\mathbf{u}}{Dt} = \frac{\partial \mathbf{u}}{\partial t} + \mathbf{u} \cdot \nabla \mathbf{u}$.

For the incompressible Navier-Stokes equations, the stress values are related to the velocity gradients and the pressure through

$$\boldsymbol{\sigma} = 2\mu \nabla^s \mathbf{u} - p\mathbf{I}, \tag{2}$$

where μ is the dynamic viscosity, p is the pressure, $\mathbf{I}$ is the identity matrix, and $\nabla^s \mathbf{u}$ is the symmetric gradient tensor of the velocity field.

Possible boundary conditions on the boundary domains are

$$\begin{cases} \overline{\boldsymbol{\sigma}}_n = \boldsymbol{\sigma}_n = (2\mu \nabla^s \mathbf{u} - p\mathbf{I}) \cdot \mathbf{n} & \text{on } \Gamma_\sigma \\ \overline{\mathbf{u}} = \mathbf{u} & \text{on } \Gamma_u, \end{cases} \tag{3}$$

where $\overline{\boldsymbol{\sigma}}_n$ and $\overline{\mathbf{u}}$ represent known external values, and $\mathbf{n}$ is the outside normal vector.

Possible internal conditions at the internal interface are

$$\boldsymbol{\sigma}_n^+ = \boldsymbol{\sigma}_n^- \quad \text{on } \Gamma_{\text{int}}, \tag{4}$$

where $\boldsymbol{\sigma}_n^+$ and $\boldsymbol{\sigma}_n^-$ represent the normal stresses on both sides of the interface considering positive in the sense of the outside unit normal to the interface, respectively.

2.2 | Conservation of mass

Mass conservation, or the continuity equation, must be satisfied in the entire fluid domain. Assuming incompressible fluid flows, continuity requires the divergence of the velocity to be zero, ie,

$$\nabla \cdot \mathbf{u} = 0, \tag{5}$$

with the following boundary conditions:

$$\mathbf{u}_n = \mathbf{u} \cdot \mathbf{n} = \overline{\mathbf{u}}_n \quad \text{on } \Gamma_u. \tag{6}$$

On the internal interfaces, the incompressible condition forces to have

$$\mathbf{u}_n^+ = \mathbf{u}_n^- \quad \text{on } \Gamma_{\text{int}}, \tag{7}$$

where, again, $\mathbf{u}_n^+$ and $\mathbf{u}_n^-$ represent the normal velocity on both sides of the interface.
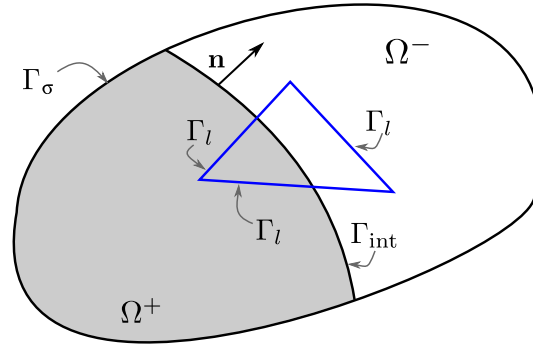
FIGURE 1 Nomenclature employed for interface names and regions [Colour figure can be viewed at wileyonlinelibrary.com]

3 ┃ THE FINITE-ELEMENT DISCRETIZATION AND THE ENRICHED SPACE

3.1 ┃ Conservation of linear momentum

In a finite-element approximation, artificial kinks of the unknown functions between 2 neighboring elements are introduced. In this case, the following constraint must be added:

$$\boldsymbol{\sigma}_n^{\text{ele}} = \boldsymbol{\sigma}_n^{\text{neigh}} \quad \text{on } \Gamma_l, \tag{8}$$

where Γ_l represents all the finite-element boundaries (see Figure 1), $\boldsymbol{\sigma}_n^{\text{ele}}$ represents the normal stresses at the finite-element boundaries, and $\boldsymbol{\sigma}_n^{\text{neigh}}$ represents the normal stresses on the finite-element boundaries of the neighboring elements.

The weighted residual form of the previous equation is

$$\sum_{\Omega_l=1}^{\Omega_{l=Ne}} \int_{\Omega_l} \mathbf{w} \cdot \left(\rho \frac{D\mathbf{u}}{Dt} - \nabla \cdot 2\mu \nabla^s \mathbf{u} + \nabla p - \mathbf{b} \right) d\Omega - \int_{\Gamma_\sigma} \mathbf{w} \cdot \left(\overline{\boldsymbol{\sigma}_n} - \boldsymbol{\sigma}_n \right) d\Gamma$$
$$- \int_{\Gamma_{\text{int}}} \mathbf{w} \cdot \left(\boldsymbol{\sigma}_n^+ - \boldsymbol{\sigma}_n^- \right) d\Gamma - \int_{\Gamma_l} \mathbf{w} \cdot \left(\boldsymbol{\sigma}_n^{\text{ele}} - \boldsymbol{\sigma}_n^{\text{neigh}} \right) d\Gamma = 0, \tag{9}$$

where $\mathbf{w}$ is the vector of weighting functions (equal to the shape function to be used to approximate the velocity field in the case of Galerkin approximations).

Remark. For a Eulerian time integration, the weighting function should be modified in order to get spatially stabilized schemes.[26]

After the integration by parts, (9) remains as follows:

$$\sum_{\Omega_l=1}^{\Omega_{l=Ne}} \left[\int_{\Omega_l} \mathbf{w} \cdot \left(\rho \frac{D\mathbf{u}}{Dt} - \mathbf{b} \right) + \nabla \mathbf{w} :: \left(\mu \nabla^s \mathbf{u} + p\mathbf{I} \right) \right] d\Omega - \int_{\Gamma_\sigma} \mathbf{w} \cdot \overline{\boldsymbol{\sigma}_n} \, d\Gamma. \tag{10}$$

Note that due to the continuity of the weighting functions $\mathbf{w}$, after integration by parts, all the integrals on the internal interfaces at the real interface Γ_{int} as well as on the artificial interelement interfaces Γ_l disappear.

Nevertheless, in order to allow the possibility of having discontinuities in the velocity field, special discontinuous shape functions will be added to the continuous standard finite-element shape functions. In the same way, a continuous part and a discontinuous part will form the weighting functions. Calling $\mathbf{w}_e$ the discontinuous weighting function to be introduced for the enriched space and maintaining the notation of $\mathbf{w}$ for the standard continuous finite-element weighting functions,

the integration by part will read as follows:

$$\sum_{\Omega_{l=1}}^{\Omega_{l=Ne}} \int_{\Omega_l} \left[\mathbf{w} \cdot \left(\rho \frac{D\mathbf{u}}{Dt} - \mathbf{b} \right) + \nabla \mathbf{w} :: \left(\mu \nabla^s \mathbf{u} + p\mathbf{I} \right) \right] d\Omega - \int_{\Gamma_\sigma} \mathbf{w} \cdot \overline{\boldsymbol{\sigma}_n} \, d\Gamma = 0$$

$$\sum_{\Omega_{l=1}}^{\Omega_{l=Ne}} \int_{\Omega_l} \left[\mathbf{w}_e \cdot \left(\rho \frac{D\mathbf{u}}{Dt} - \mathbf{b} \right) + \nabla \mathbf{w}_e :: \left(\mu \nabla^s \mathbf{u} + p\mathbf{I} \right) \right] d\Omega - \int_{\Gamma_\sigma} \mathbf{w}_e \cdot \overline{\boldsymbol{\sigma}_n} \, d\Gamma$$

$$- \int_{\Gamma_{\text{int}}} \left(\mathbf{w}_e^+ \cdot \boldsymbol{\sigma}_n^- + \mathbf{w}_e^- \cdot \boldsymbol{\sigma}_n^+ \right) d\Gamma - \int_{\Gamma_l} \mathbf{w}_e \cdot \boldsymbol{\sigma}_n^{\text{neigh}} \, d\Gamma = 0. \tag{11}$$

The first line in (11) is the standard variational form for the continuous weighting functions $\mathbf{w}$, whereas the second line is the variational form for discontinuous weighting functions.

The term σ_n^{neigh} represents the normal stress to the finite-element boundaries of the neighboring elements, and σ_n^+, $\mathbf{w}_e^+$, σ_n^-, and $\mathbf{w}_e^-$ are the normal stress and the enriched weighting function on both sides of the internal interface. The evaluation of these terms will be discussed later.

3.2 | Conservation of mass

As stated before, the elemental enriched space may introduce discontinuities between the 2 neighboring elements as well in the velocity field as in the pressure field. Furthermore, for a Galerkin approximation, the corresponding weighting functions have exactly the same possible discontinuities that must be taken into account in order to satisfy the incompressible condition.

Possible velocity discontinuities between elements force to impose the following constraint:

$$\mathbf{u}_n^{\text{ele}} = \mathbf{u}_n^{\text{neigh}} \quad \text{on } \Gamma_l, \tag{12}$$

where $\mathbf{u}_n^{\text{ele}}$ represents the normal velocity to a boundary element, and $\mathbf{u}_n^{\text{neigh}}$ represents the normal velocity on the boundary of the neighboring element.

The weighted residual form of the mass conservation with possible discontinuous velocity fields (supposing that the boundary constraint $\mathbf{u}_n = \overline{\mathbf{u}}_n$ is a priori satisfied) reads:

$$\sum_{\Omega_{l=1}}^{\Omega_{l=Ne}} \left[\int_{\Omega_l} w^p \nabla \cdot \mathbf{u} \, d\Omega - \int_{\Omega_l} \nabla w^p \cdot \mathbf{u}_e \, d\Omega + \int_{\Gamma_\mathbf{u}} w^p \overline{\mathbf{u}}_{ne} \, d\Gamma + \int_{\Gamma_{\text{int}}} w^p \left(\mathbf{u}_{ne}^+ - \mathbf{u}_{ne}^- \right) d\Gamma + \int_{\Gamma_l} w^p \left(\mathbf{u}_{ne}^{\text{neigh}} - \mathbf{u}_{ne}^{\text{ele}} \right) d\Gamma \right] = 0, \tag{13}$$

where w^p is the weighting function equal to the shape function to be used to approximate the pressure field in the case of Galerkin approximations, and $\overline{\mathbf{u}}_{ne}$ is the enriched velocity at the boundary.

Remark. Equal-order interpolation for velocity pressure is stabilized through streamline-upwind/pressure-stabilizing Petrov-Galerkin methods in this context.

For the case of continuous velocity fields, all the boundary integrals in the previous equation disappear, but for discontinuous velocities, special care must be taken on the internal interfaces and on the boundaries between 2 neighboring elements crossed by the interface.

Furthermore, the pressure (and then the weighting functions w^p) will be also enriched with discontinuous functions. Calling w^p the continuous weighting functions for the incompressible terms and $\mathbf{u}_e$ and w_e^p the enriched velocity shape functions and the pressure weighting functions, respectively, 4 cases must be taken into consideration.

1. *Continuous weighting functions and continuous velocity shape functions.* In this case, the weighted residual form for the incompressible equation reduces to

$$\sum_{\Omega_{l=1}}^{\Omega_{l=Ne}} \left[\int_{\Omega_l} w^p \nabla \cdot \mathbf{u} \, d\Omega \right] = 0. \tag{14}$$

2. *Continuous pressure weighting functions and discontinuous velocity shape functions.* In this case, integrating by parts the divergence term, all the boundary integral terms disappear, producing

$$- \sum_{\Omega_{l=1}}^{\Omega_{l=Ne}} \left[\int_{\Omega_l} \nabla w^p \cdot \mathbf{u}_e \, d\Omega \right] + \int_{\Gamma} w^p \cdot \mathbf{u}_{ne} \, d\Gamma = 0. \tag{15}$$

This means that the terms involved in continuous pressure weighting functions and discontinuous velocity shape functions are easily solved integrating by parts the divergence velocity term. In contrast, an integral term must be added in the whole external contour of the domain.

3. *Discontinuous weighting functions and continuous velocity shape functions.* In this case, again, (13) reduces to

$$\sum_{\Omega_{l=1}}^{\Omega_{l=Ne}} \left[\int_{\Omega_l} w_e^p \nabla \cdot \mathbf{u} \, d\Omega \right] = 0. \tag{16}$$

4. *Discontinuous weighting functions and discontinuous velocity shape functions.* In this case, Equation (13) remains with all the terms. Integration by parts avoids some terms on the boundary integrals, but the terms concerning the neighboring elements remain in the equation, which makes it impossible to be exactly solved with an elemental enrichment strategy. The approximation of both neighboring terms $\boldsymbol{\sigma}_n^{\text{neigh}}$ in (11) and $\mathbf{u}_n^{\text{neigh}}$ in (13) will be discussed next.

4 | EVALUATION OF THE JUMP CONDITION FOR THE INTERNAL INTERFACES

Equation (11) introduces integral terms with the normal stresses $\boldsymbol{\sigma}_n^+$ and $\boldsymbol{\sigma}_n^-$, which represent the normal stresses on both sides of the internal interface in which a jump or a kink might be located. To evaluate these terms, a regularization zone on a very thin band with thickness ϵ will be considered. On this band, the stress tensor will be described in local coordinates on the interface in its normal and tangent directions n, τ_1, and τ_2, respectively, which will be named $\boldsymbol{\sigma}^R$. In the same way, the normal unit vector in these particular coordinates will be called $\mathbf{n}^R$ with $(\mathbf{n}^R)^T = (1, 0, 0)$. For instance, for the 2D case, the matrix $\boldsymbol{\sigma}^R$ remains as follows:

$$\boldsymbol{\sigma}^R = 2\boldsymbol{\mu}^* \begin{bmatrix} \frac{\partial \mathbf{u}_n}{\partial n} & \frac{1}{2} \left(\frac{\partial \mathbf{u}_\tau}{\partial n} + \frac{\partial \mathbf{u}_n}{\partial \tau} \right) \\ \frac{1}{2} \left(\frac{\partial \mathbf{u}_\tau}{\partial n} + \frac{\partial \mathbf{u}_n}{\partial \tau} \right) & \frac{\partial \mathbf{u}_\tau}{\partial \tau} \end{bmatrix} - p\mathbf{I}. \tag{17}$$

The coefficient $\boldsymbol{\mu}^*$ is a fictitious viscosity of the regularization zone. It can be considered as an orthotropic material. Thus

$$\boldsymbol{\mu}^* = \begin{bmatrix} \mu_n^* & 0 \\ 0 & \mu_\tau^* \end{bmatrix}. \tag{18}$$

The tensor stress normal to the interface in the regularized region becomes

$$\boldsymbol{\sigma}_n^R = \boldsymbol{\sigma}^R \cdot \mathbf{n}^R = 2 \begin{bmatrix} \mu_n^* & 0 \\ 0 & \mu_\tau^* \end{bmatrix} \begin{bmatrix} \frac{\partial \mathbf{u}_n}{\partial n} \\ \frac{1}{2} \left(\frac{\partial \mathbf{u}_\tau}{\partial n} + \frac{\partial \mathbf{u}_n}{\partial \tau} \right) \end{bmatrix} - p\mathbf{n}^R. \tag{19}$$

Furthermore, in this region, the derivatives in the direction of the normal to the interface may be written as

$$\frac{\partial \mathbf{u}_n^R}{\partial n} = \frac{\|\mathbf{u}_n\|^+}{\epsilon} \quad \text{and} \quad \frac{\partial \mathbf{u}_\tau^R}{\partial n} = \frac{\|\mathbf{u}_\tau\|^+}{\epsilon}, \tag{20}$$

where $\|\mathbf{u}_\alpha\|^+ = \mathbf{u}_\alpha^+ - \mathbf{u}_\alpha^-$ and $\|\mathbf{u}_\alpha\|^- = \mathbf{u}_\alpha^- - \mathbf{u}_\alpha^+$ represent the jumps at the interface of the α component of the velocity including the sign.

For a finite value of the jumps, this derivative tends to infinity when ϵ tends to zero. This means that the other derivatives may be neglected on this regularized region, ie,

$$\boldsymbol{\sigma}_n^{R+} = 2 \begin{bmatrix} \mu_n^* & 0 \\ 0 & \mu_\tau^* \end{bmatrix} \begin{bmatrix} \frac{\|\mathbf{u}_n\|^+}{\epsilon} \\ \frac{\|\mathbf{u}_\tau\|^+}{2\epsilon} \end{bmatrix} - p^+ \mathbf{n}^R$$

$$= 2 \begin{bmatrix} \frac{\mu_n^*}{\epsilon} & 0 \\ 0 & \frac{\mu_\tau^*}{2\epsilon} \end{bmatrix} \|\mathbf{u}^R\|^+ - p^+ \mathbf{n}^R = \mathbf{J}^R \|\mathbf{u}^R\|^+ - p^+ \mathbf{n}^R, \tag{21}$$

where the orthotropic coefficient matrix $\mathbf{J}^R$ is

$$\mathbf{J}^R = \begin{bmatrix} J_n & 0 \\ 0 & J_\tau \end{bmatrix} = \begin{bmatrix} \frac{2\mu_n^*}{\epsilon} & 0 \\ 0 & \frac{\mu_\tau^*}{\epsilon} \end{bmatrix}. \tag{22}$$

Taking into account all the previous considerations, the normal stress at the interface $\boldsymbol{\sigma}_n^+$ must be evaluated as

$$\boldsymbol{\sigma}_n^+ = \boldsymbol{\sigma}_n \cdot \mathbf{n}^+ = \mathbf{R}^T \boldsymbol{\sigma}^R \mathbf{R} \mathbf{R}^T \cdot \mathbf{n}^R = \mathbf{R}^T \boldsymbol{\sigma}^R \cdot \mathbf{n}^R = \mathbf{R}^T \boldsymbol{\sigma}_n^R = \mathbf{R} \left(\mathbf{J}^R \|\mathbf{u}^R\|^+ - p^+ \mathbf{n}^R \right) \tag{23}$$

or

$$\boldsymbol{\sigma}_n^+ = \mathbf{R}^T \mathbf{J}^R \mathbf{R} \|\mathbf{u}\|^+ - p^+ \mathbf{R}^T \cdot \mathbf{n}^R = \mathbf{J} \|\mathbf{u}\|^+ - p^+ \mathbf{n}^+, \tag{24}$$

with $\mathbf{J} = \mathbf{R}^T \mathbf{J}^R \mathbf{R}$ and $\mathbf{R}$ as the rotation tensor. Note that, according to their definition from fictitious viscosities, both J_n and J_τ regulate the amount of momentum transfer in the regularization zone along normal and tangential directions, respectively, and the degree of continuity in the primal variables. In this context, a zero value of any of these coefficients implies no momentum transfer between regions along their respective directions and, therefore, some discontinuity in the primitive variable. On the contrary, an infinite value indicates total momentum transfer, ie, momentum continuity.

As a summary, the final equations to be solved are as follows.

1. *Momentum conservation*

$$\sum_{\Omega_{l=1}}^{\Omega_{l=Ne}} \int_{\Omega_l} \left[\mathbf{w} \cdot \left(\rho \frac{D\mathbf{u}}{Dt} - \mathbf{b} \right) + \nabla \mathbf{w} :: \left(\mu \nabla^s \mathbf{u} + p\mathbf{I} \right) \right] d\Omega - \int_{\Gamma_\sigma} \mathbf{w} \cdot \overline{\boldsymbol{\sigma}_n} \, d\Gamma = 0$$

$$\sum_{\Omega_{l=1}}^{\Omega_{l=Ne}} \int_{\Omega_l} \left[\mathbf{w}_e \cdot \left(\rho \frac{D\mathbf{u}}{Dt} - \mathbf{b} \right) + \nabla \mathbf{w}_e :: \left(\mu \nabla^s \mathbf{u} + p\mathbf{I} \right) \right] d\Omega - \int_{\Gamma_\sigma} \mathbf{w}_e \cdot \overline{\boldsymbol{\sigma}_n} \, d\Gamma$$

$$- \int_{\Gamma_{\text{int}}} \left(\mathbf{w}_e^+ \cdot \left(\mathbf{J} \|\mathbf{u}\|^+ - p^+ \mathbf{n}^+ \right) + \mathbf{w}_e^- \cdot \left(\mathbf{J} \|\mathbf{u}\|^- - p^- \mathbf{n}^- \right) \right) d\Gamma - \int_{\Gamma_l} \mathbf{w}_e \cdot \boldsymbol{\sigma}_n^{\text{neigh}} \, d\Gamma = 0 \tag{25}$$

2. *Mass conservation*

$$\sum_{\Omega_{l=1}}^{\Omega_{l=Ne}} \left[\int_{\Omega_l} w^p \nabla \cdot \mathbf{u} \, d\Omega - \int_{\Omega_l} \nabla w^p \cdot \mathbf{u}_e \, d\Omega \right] + \int_\Gamma w^p \cdot \mathbf{u}_{ne} \, d\Gamma = 0$$

$$\sum_{\Omega_{l=1}}^{\Omega_{l=Ne}} \left[\int_{\Omega_l} w_e^p \nabla \cdot (\mathbf{u} + \mathbf{u}_e) \, d\Omega + \int_{\Gamma_{\text{int}}} \left(w_e^{p+} \|\mathbf{u}_e\|^+ \cdot \mathbf{n}^+ + w_e^{p-} \|\mathbf{u}_e\|^- \cdot \mathbf{n}^- \right) d\Gamma + \int_{\Gamma_l} w_e^p \left(\mathbf{u}_{ne}^{\text{neigh}} - \mathbf{u}_{ne}^{\text{ele}} \right) d\Gamma \right] = 0 \tag{26}$$

It must be noted that in case the integration by parts of the terms involved with the continuous weighting functions and the discontinuous enriched functions (second integral in the first line of (26)) is not performed, then the first line of (26) remains as follows:

$$\sum_{\Omega_{l=1}}^{\Omega_{l=Ne}} \left[\int_{\Omega_l} w^p \nabla \cdot (\mathbf{u} + \mathbf{u}_e) \, d\Omega - \int_{\Gamma_{\text{int}}} w^p \|\mathbf{u}_e\| \cdot \mathbf{n} \, d\Gamma + \int_{\Gamma_l} w^p \left(\mathbf{u}_{ne}^{\text{neigh}} - \mathbf{u}_{ne}^{\text{ele}} \right) d\Gamma \right] = 0, \tag{27}$$

which means that without this integration by parts, one integral must be added on the internal interfaces and along all the element boundaries enriched in order to preserve the mass conservation.

In the previous equations, there are terms named σ_n^{neigh} and $\mathbf{u}_n^{\text{neigh}}$ corresponding to the normal stress and normal velocity of the neighboring element where the integration is performed. In order to enable the condensation of the enriched DOF at the elemental level (EFEM), these 2 terms will be approximated with the corresponding stress and velocity in the integration element itself. In other words, $\sigma_n^{\text{neigh}} = \sigma_n^{\text{ele}}$ and $\mathbf{u}_{ne}^{\text{neigh}} = \mathbf{u}_{ne}^{\text{ele}}$.

With this approximation, the last integral on the element boundaries of the mass conservation equations becomes null, producing only the last integral on the element boundaries in the momentum equation. These integrals were named *interelement forces* in the previous work of the authors[1] because they are similar to the introduction of a load on both boundaries of 2 neighboring elements. However, as explained in the aforementioned work,[1] the addition of these integrals must not be understood as the addition of a boundary load. It must be better interpreted as a *do nothing* boundary condition between the 2 neighboring elements. The *do nothing* boundary condition was first proposed in the work of
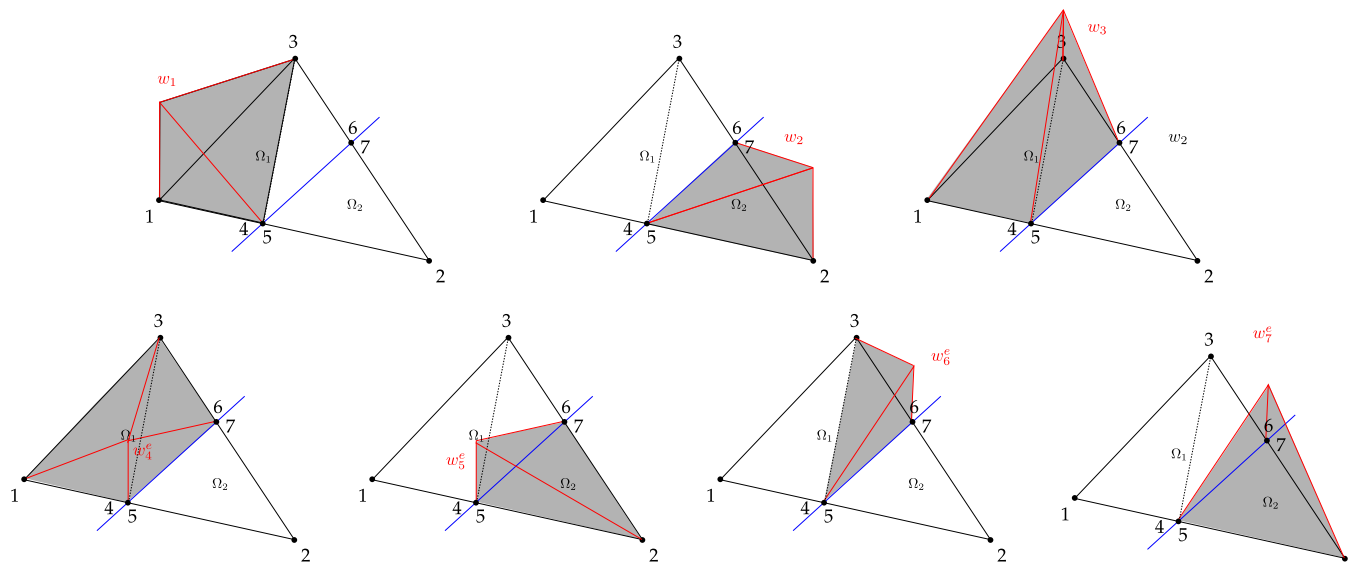
FIGURE 2 Standard and enriched shape functions for a kink and a jump: 2-dimensional case [Colour figure can be viewed at wileyonlinelibrary.com]

Papanastasiou et al[27] to improve the outflow boundary condition in unbounded flows. It was later generalized to a slip boundary condition in the work of Behr[28] and discussed in the work of Coppola-Owen and Codina.[29] In this new enriched space, the *do nothing* boundary condition will improve the capture of the discontinuity existing between 2 elements in the case of elemental enrichment. As can be seen in the numerical examples, these interelement forces considerably improve the accuracy of elemental enrichment, decreasing (and, in many cases, eliminating) the artificial jump that appears between 2 neighboring elements due to the static condensation of the enriched DOF.

Unfortunately, in spite of using a Galerkin approximation, the interelement forces and the integration by parts of one of the terms in the mass conservation equation generate a nonsymmetry stiffness matrix. Nevertheless, the improvements in the results that are obtained using this approximation counteract the disadvantage of having asymmetric matrices.

5 | THE FINITE ELEMENT WITH THE ENRICHED SHAPE FUNCTION

The enriched space for reproducing a kink or a jump inside a 2D triangle may be obtained by subdividing the element in 3 subelements and using the standard finite-element shape functions of each subelement, as shown in Figure 2.

For the case of kinks + jumps, the triangle is subdivided in the same way, but the nodes at the internal interface are duplicated. The procedure to obtain the final stiffness matrix of each element to be assembled in the global stiffness matrix may be followed in the previous work of the authors.[1]

The stiffness matrix of each subelement is assembled in 1 superelement of 5 nodes (for kinks) or 7 nodes (for kinks + jumps). The interelemental forces are added on all the element boundaries in which an internal interface is present. Finally, the enriched DOFs are eliminated by static condensation following a standard procedure presented in Appendix.

In the case of 3D finite elements, the internal interfaces are composed of planar facets, which do not conform to the element faces. Again, the element can then be split into 2 subregions. Two possible situations have to be considered, since the reconstructed interface can be either a triangular or a quadrangular facet. In the first case, the tetrahedron is subdivided into 4 subelements, and in the second case, it is divided into 6 subelements. Then, the enriched DOFs are eliminated by static condensation as usual.

Two different cases of the pathological problem have been referred in the previous paper, and the same solution will be used now. One case is related to geometrical problems involved when the internal interface is near a node, very close to an interface, or both. The other case is related to which decision must be taken when there are more than one result in the same position as currently occur in the elemental enriched space. The readers are referred to the previous paper in order to learn about the solution adopted for both cases.
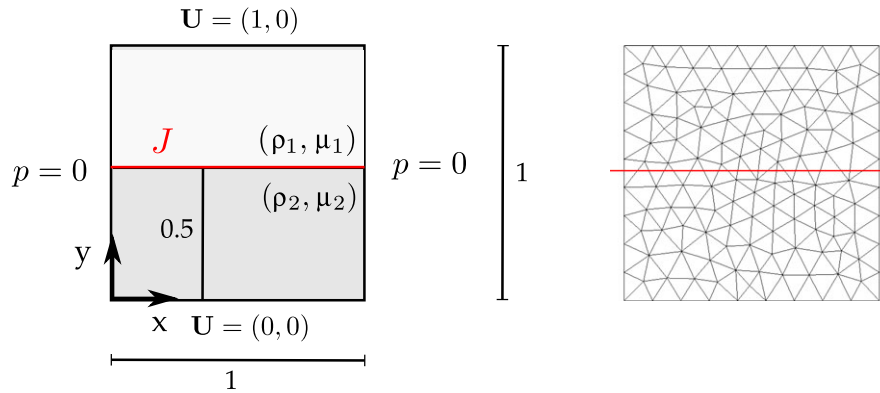
FIGURE 3 Couette flow case configuration and unstructured mesh employed. The units are m/s for velocity, Pa for pressure, Pa·s for viscosity, and kg/m^3 for density [Colour figure can be viewed at wileyonlinelibrary.com]

Concerning the inertial terms $\int_{\Omega_l} \mathbf{w} \cdot \rho \frac{D\mathbf{u}}{Dt} \, d\Omega$, the enrichment space was not considered, using for these terms the standard finite-element shape functions corresponding to the linear triangle or the lineal tetrahedral, respectively. For the case of a Eulerian formulation, the term $\frac{D\mathbf{u}}{Dt}$ was replaced by $\frac{\partial \mathbf{u}}{\partial t} + \mathbf{u} \cdot \nabla \mathbf{u}$ with a standard streamline-upwind Petrov-Galerkin stabilized scheme[26] without any enriched space used to avoid spurious oscillation due to the convective terms.

It must be also noted that in the case of equal-order velocity pressure elements as those used in the examples presented next, the conservation of mass equation must be also stabilized. A standard pressure-stabilizing Petrov-Galerkin[26] stabilization was used here without enrichment in its functional space.

6 | NUMERICAL EXAMPLES

The numerical examples chosen in this section are fluid mechanics problems where the unknown functions are the velocity and pressure fields. The main objective is to highlight the possibilities of the EFEM for these kinds of vectorial solutions and put in evidence the accuracy of the elemental enrichment in this context. To see the errors compared with analytical solutions and the convergence of the method for more academic cases, the readers are referred to the authors' previous work.[1]

6.1 | Couette flow with 2 fluids

The first case analyzed is the incompressible flow counterpart of the cases named *one-dimensional kink* and *one-dimensional jump* presented in the previous work of the authors.[1] Instead of solving thermal problems, in the current case, the unknowns are the velocity and pressure fields. According to the geometry and boundary conditions presented in Figure 3, the test represents the problem of 2 plane plates with different tangential velocities between them, also known as the Couette flow. If the same fluid at each side of the interface is considered and $J_\tau = J_n = \infty$ is imposed, the solution is the classical linear velocity profile. In the case of fluids with different viscosities, a kink of the velocity is produced on the interface due to a discontinuity in their gradients. The analytical solution is presented in (28), while the pressure is constant over all the domains, taking the same value imposed at the inlet.

$$\mathbf{u}_x(x,y) = \begin{cases} \frac{2\mu_2}{\mu_1 + \mu_2} y & y \leq 0.5 \\ 1 - \frac{2\mu_1}{\mu_1 + \mu_2}(1-y) & y > 0.5 \end{cases} \tag{28}$$

The first test considers a viscosity jump of $\mu_1 = 1$, $\mu_2 = 10$ with constant density $\rho_1 = \rho_2 = 1$ and continuity of the solution at the interface, ie, $J_\tau = J_n = \infty$. Figure 4 A presents the analytic solution over a slice at $x = 1$ compared with 3 different numerical solutions obtained employing the unstructured mesh showed in Figure 3. The solution with a standard finite-element method, ie, without enrichment, fails at capturing the kink and wrongly estimates the velocity gradient, which results in an unacceptable solution even in this simple case. As expected, using enrichment improves kink capturing. However, as discussed before in this work, the lack of the interelemental load term leads to a solution that
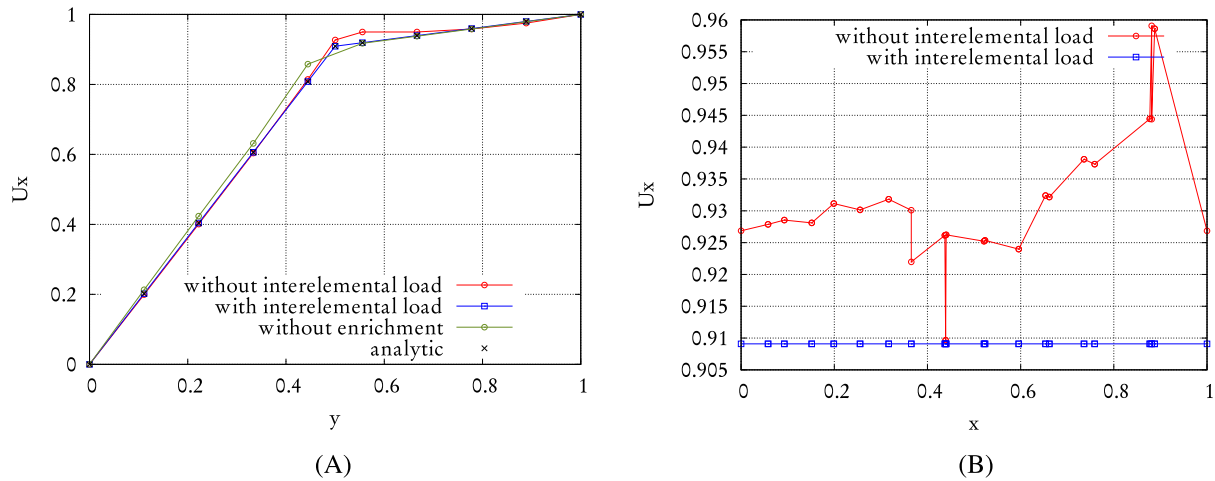
FIGURE 4 Couette flow with a kink generated by a viscosity jump. Horizontal velocity over horizontal and vertical slices. A, $x = 1$ slice; B, $y = 0.5$ slice [Colour figure can be viewed at wileyonlinelibrary.com]
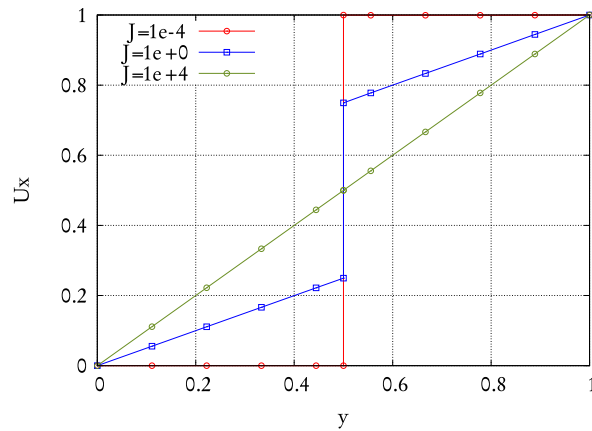

FIGURE 5 Couette flow with a jump. Solutions for different values of J [Colour figure can be viewed at wileyonlinelibrary.com]

has some deficiencies specially in the region of small viscosity. That variational crime is clearly solved incorporating the mentioned term in the elemental assemble (solution with interelemental load). This difference is highlighted in Figure 4B, where the value of x-velocity over the enriched DOFs over the interface is presented. It is noticeable how including the interelemental load the solution obtained matches the analytic one, whereas not employing it results in the solution being poor. Moreover, some enriched nodes at the same physical point have different velocity values depending on the interface side where they are. As seen in this first case, the only numerical strategy that guarantees an accurate solution when the mesh does not match the interface is employing enrichment with interelemental load.

The second example considers a jump in the unknowns. A jump of the velocity in an incompressible flow problem may be considered when there are 2 fluids in contact but supposing that there is a material in between the 2 domains that imposes some restriction for momentum transference. It is, for instance, how the surface tension acts at the interface of 2 fluids or the presence of a plate between 2 fluids with the same or different physical properties. The amount of momentum transfer for each direction, ie, tangential and normal to the interface, is regulated by the coefficient of the matrix **J** described in (22). Although J_n can take any value depending on the problem, in this case and the following ones in this work, we will always consider the same normal velocity at both sides of the interface with $J_n = \infty$. Cases with $J_n \neq \infty$ are not treated in this work, but could be useful in the case of curved interfaces where a slipping condition should be ensured, but as the interface is represented by straight lines, a locking of the flow is found at the interface. Therefore, in order to simplify the notation, we will use J when we refer to J_τ.

Figure 5 compares the solutions in a problem with the same fluid at both sides of the interface ($\mu_1 = \mu_2 = \rho_1 = \rho_2 = 1$) when J varies. In all the cases, the enrichment proposed with the interelemental forces gives the exact result in any horizontal line.
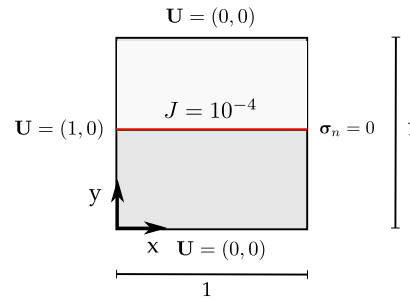
FIGURE 6 Geometry and boundary conditions for the flap valve case. The red line represents the valve position at $t = 0$ [Colour figure can be viewed at wileyonlinelibrary.com]

Remark 1. Is important to mention that the interelemental load evaluation on the edges where $\Gamma_l \cap \Gamma_\sigma \neq \emptyset$ must consider $\sigma_n^{\text{neigh}} = \bar{\sigma}_n$, ie, the traction is dictated by the boundary condition. On the other hand, for boundaries where $\Gamma_l \cap \Gamma_{\mathbf{u}} \neq \emptyset$, an approximation employing $\sigma_n^{\text{neigh}} = \sigma_n^{\text{ele}}$ is adopted as in the internal edges.

Remark 2. In contrast to the previous work[1] where linear equation systems were solved, in the case of incompressible flows, nonlinear systems must be solved. In this context, the condensation of new DOFs introduces nonlinearities that must be solved iteratively. Therefore, previous iteration values for enriched nodes must be stored. During the first nonlinear iteration, linear interpolation among parent nodes could be considered to impose an initial value on enriched nodes. Note that even if the solution for the velocity field on each phase is a linear profile, the equation system solved includes the convective nonlinear term, and the use of condensed unknowns forces to iterate the linearized solver.

6.2 | Moving flap valve

The Couette case shows the capability of the enriched space proposed to improve the accuracy of the solution when a coarse mesh does not match the interface and there is a kink or/and a jump of the unknowns. However, if the interface position is fixed, a matching mesh (with duplicated nodes at the interface) can be used or strategies as XFEM can be applied, and the accuracy of the results will be at least equal.

In this context, this case proposes a moving interface where a matching mesh strategy would require remeshing every time step, or the matrix of the equation system of XFEM techniques should be resized according to the variation in positioning and the number of extra DOFs. This task requires extensive computational time, which can be avoided if the EFEM proposal of this work is employed, where exactly the same matrix graph is used; this means that the solution matrix has exactly the same DOFs although the interface position may be continuously moving.

Figure 6 shows a 2D homogeneous and incompressible flow problem that represents a pipe with a flap valve characterized by a moving interface. The valve position is fixed at the inlet, and a rigid oscillating movement is imposed following the equation: $y(x, t) = 0.5 + x0.15 \sin(2\pi t/T)$. Imposing impenetrability, ie, $\mathbf{u}_n|_{\Gamma_{\text{int}}} = 0$, and discontinuity of tangential velocities over it, ie, $J = 0$, the interface models a solid and slip valve. The flow rate imposed at the inlet is 1 m³/s, and it must be kept constant at the outlet; this condition will accelerate the flow in the region where the valve constrains its area.

The background fixed mesh employed consists in 36×18 structured nodes conforming 1296 triangles. The oscillation period is $T = 10^5$, whereas the time step employed is $\Delta t = 5 \times 10^3$. These huge temporal steps are selected in order to avoid the influence of the mass matrix over the system. In this context, each time step is treated as a pseudo-stationary state.

Figure 7 shows the magnitude of the velocity at different valve positions. As a validation of the results, the difference between the inlet flow rate and the outlet flow rate is considered. Maximum differences are about 1% and could be attributed to the coarse background mesh employed. This fact can be observed in the comparison among the velocity profiles at the outlet shown in Figure 8. When the valve is centered (for example, at the starting position), the solution is the classical parabolic profile with maximum $|\mathbf{u}|_{\max} = \frac{3}{2}|\mathbf{u}|_{\text{inlet}}$. Solutions for other stages present a jump at the interface, and the velocity varies its maximum according to the contraction or expansion of the region transversal area, in order to guarantee conservativeness.

Remark 3. In this case, a slip condition is employed over the interface. A possible improvement could be including the modeling of a boundary layer through a wall law, adjusting the value of J.
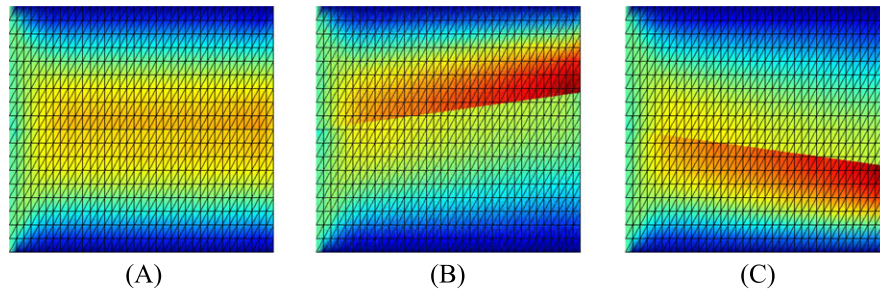
FIGURE 7 Moving-valve case. |**u**| at several snapshots. Scale from |**u**| = 0 m/s (blue) to |**u**| = 2.2 m/s (red). A, $t^* = 0$; B, $t^* = 1/4$; C, $t^* = 3/4$ [Colour figure can be viewed at wileyonlinelibrary.com]
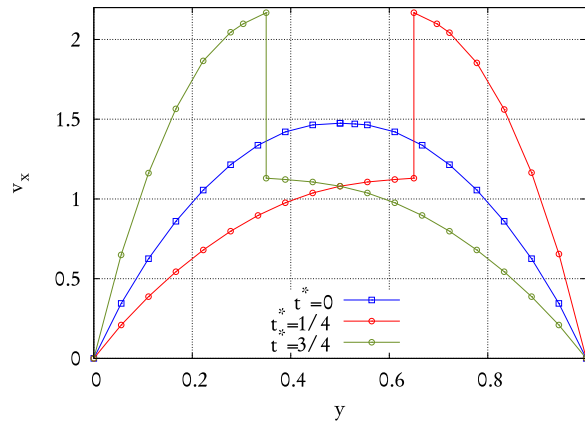

FIGURE 8 Moving-valve case. Velocity profile at the outlet ($x = 1$) for different valve positions [Colour figure can be viewed at wileyonlinelibrary.com]

6.3 | Elbow with internal wall

The basis of this case is similar to the previous one. The flow inside a 2D pipe with a valve is also calculated. However, in this case, the pipe geometry presents a 90° curve conforming an elbow. This more complex case is employed to validate the quality of the elemental approximations used when the interface is not a straight line.

With the aim of reproducing the procedure on general simulations, instead of using the analytical expression, a distance function field $\psi(\mathbf{x})$ that has values over the mesh nodes is employed to determine the interface position. Using the standard linear shape functions, an interface element estimates the interface position as the straight line, which accomplishes $\psi(\mathbf{x}) = 0$. More details about this standard algorithm can be found in the work of Gimenez and González.[30] This procedure makes that, over a curve, the interface normals **n** vary element by element. This fact could introduce discrepancies of the unknown values computed by the pair of enriched DOFs at the same position but on different elements.

Figure 9 presents the geometry and boundary conditions employed. Note that the radius of the duct is not constant, then the interface position reduces the transversal area of the lower region after the curve. Three Cartesian grids are employed, starting from a coarse mesh with 2400 elements, which is refined by splitting each element into 4 once (medium mesh with 9600 elements), twice (fine mesh with 38 400 elements), and thrice (very fine mesh with 153 600 elements). A 1-phase flow is considered with viscosity and density of unity for simplicity. Taking as the reference length the radius of the duct, the Reynolds number simulated is Re= 1.

Pressure and velocity solutions using the coarse mesh are shown in Figure 10. The contraction in the right region of the pipe after the curve generates acceleration of the fluid in order to keep the total flow rate constant. The pressure field also presents a jump along the interface, which is expected due to the different driving forces required by each region in order to satisfy the inlet flow imposed. In this context, the inlet flow rate of 2 m³/s, which is split at the centerline of the duct into 2 equal parts, must be preserved at the outlet. Because the transversal area after the curve changes, it can be demonstrated that, considering the parabolic flow at both sides, the analytical maximum of the velocity must be 1.5 and 3 m/s in the upper (left) and lower (right) regions, respectively.
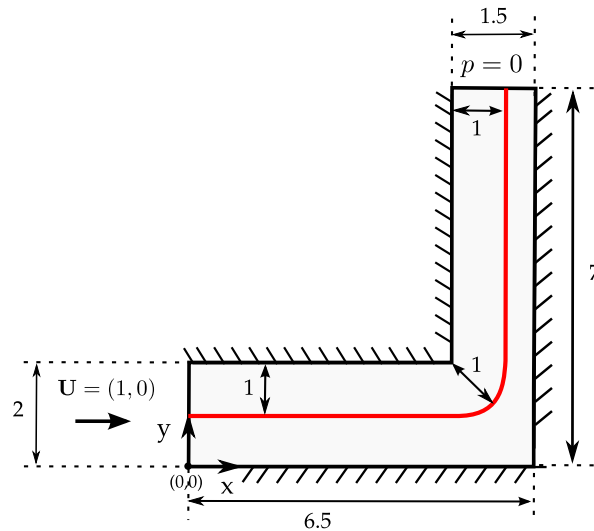
FIGURE 9 Elbow case. Geometry and boundary conditions. The red line represents the interface position [Colour figure can be viewed at wileyonlinelibrary.com]
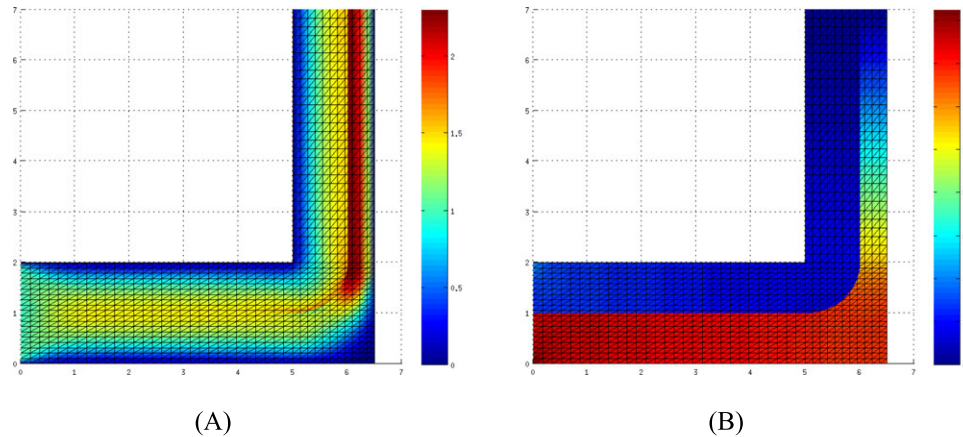

| (A) | (B) |

FIGURE 10 Elbow case. Solutions using the coarse mesh. A, Velocity magnitude; B, Pressure [Colour figure can be viewed at wileyonlinelibrary.com]

Figure 11A presents the velocity profile at a slice near the inlet ($x = 2$) compared with the velocity profile at the outlet, computed using the coarse mesh. It can be noticed how the symmetrical distribution near the inlet is modified after the curve because the duct contraction leads to a velocity jump at the interface to preserve the flow rate. Penetrability of the interface because of the procedure for computing the normals and other numerical issues, particularly for the coarse mesh, leads to solutions with a certain level of error, for example, a slower velocity at the left region of the outlet.

In order to check how the solution is improved when the mesh is refined, Figure 11B shows the velocity profile at the outlet computed by the 4 different grids employed. Measuring the error for each solution as the difference between the analytical and the numerical maximum of the parabolic profile at each side of the interface, the numerical method does not modify its error convergence order even when employing the EFEM space proposed in this work (upwind schemes are used for the convective term). Quantitative data are presented in Table 1.

6.4 | The flow through a moving sail of a sailboat

An interesting application case of the enrichment space proposed is presented here where the flow around a sailboat is simulated. The sail, an impenetrable, thick, and deformable material, is modeled as an interface with discontinuity in both normal and tangential velocities, which implies that the flow at one side does not interact directly with the flow at the other side of the sail.
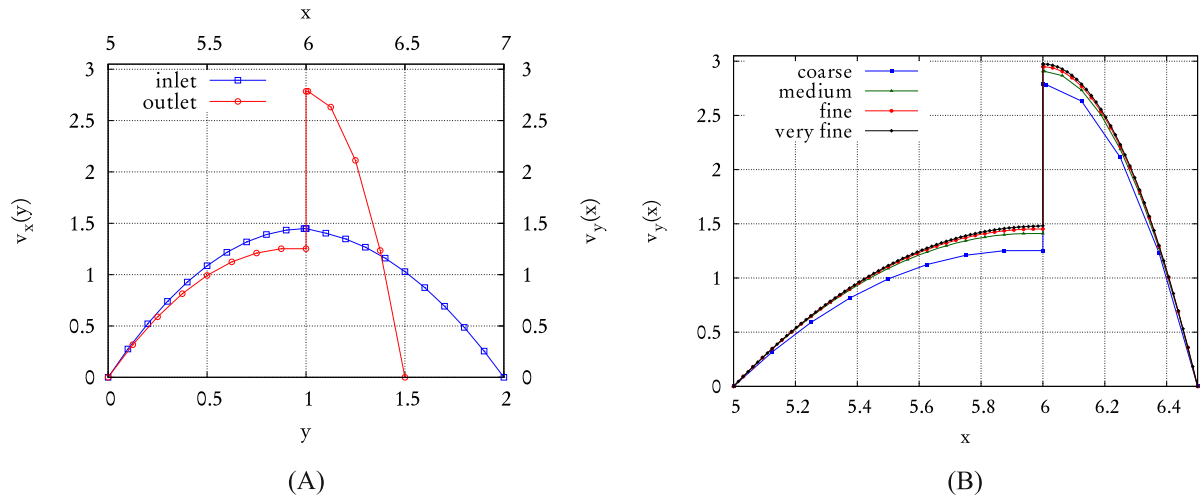
FIGURE 11 Elbow case. Velocity profiles. A, Velocity profile at the inlet and the outlet with the coarse mesh; B, Velocity profile at the outlet with several mesh refinements [Colour figure can be viewed at wileyonlinelibrary.com]

TABLE 1 Elbow case. Maximum of velocity (m/s) at the outlet using different meshes

	$|v_y|_{max}$ at Left	e	$|v_y|_{max}$ at Right	e
Expected	**1.5**	**–**	**3.0**	**–**
Coarse	1.253	0.247	2.786	0.214
Medium	1.41	0.09	2.907	0.093
Fine	1.452	0.048	2.949	0.0502
Very fine	1.4814	0.0186	2.974	0.0261
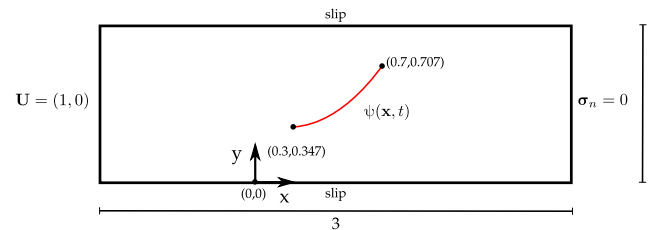
FIGURE 12 Geometry and boundary conditions for the sail case. The red line represents the sail position at $t = 0$ [Colour figure can be viewed at wileyonlinelibrary.com]

The case configuration is shown in Figure 12. The sail position is represented by the analytic function $\psi(x, t) = ax^2 + bx + c$ with $\psi(0.3) = 0.347$, $\psi(0.7) = 0.707$, and $c = \frac{3}{2} \sin(2\pi t/T)$. A uniform Cartesian grid of 75×25 elements subdivided into triangles is employed. A 1-phase flow is considered, its properties being $\mu = 1$ and $\rho = 1$. Therefore, Re = 1 taking as reference length the channel width. In order to model that the interface begins and ends inside the domain, the jump coefficient is given as follows:

$$
J = \begin{cases} 0, & 0.3 \leq x \leq 0.7 \\ \infty, & \text{otherwise.} \end{cases}
\tag{29}
$$

The solution is presented in Figure 13. Figures 13A and 13B show the magnitude of the velocity and the pressure fields, respectively, with arrows representing the direction of the flow. Although the Reynolds number of the problem is low and, thus, the flow does not produce shedding, the velocity and pressure fields have the expected features. Pressure is at maximum over the side of impact of the sail, whereas the minimum occurs behind the sail where flow detachment is observed. Flow surrounds properly the shape without permeabilities. The snapshots shown in Figure 13C-H, which present the behavior of the flow for the different positions of the sail, also accomplish the mentioned features.
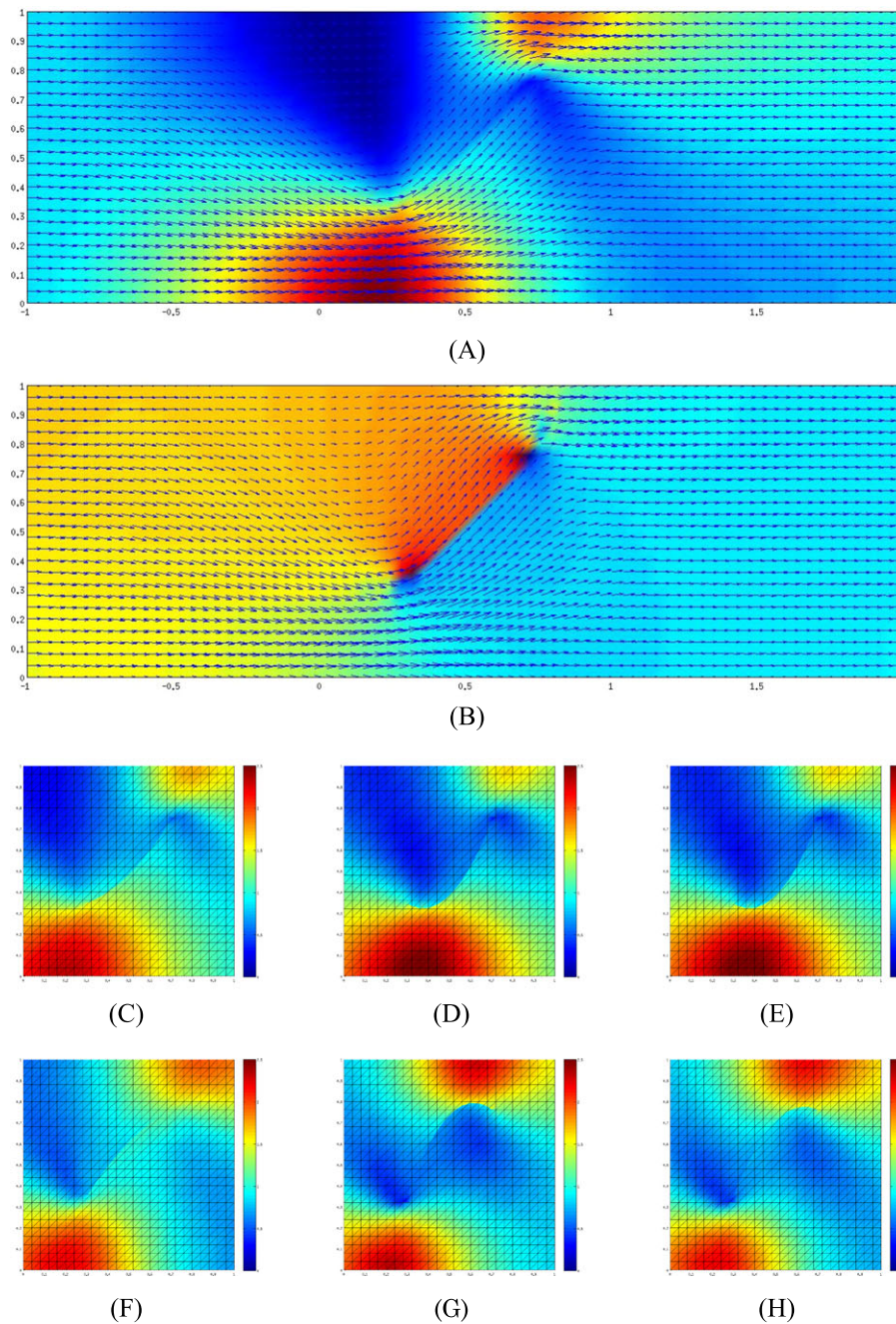
FIGURE 13 Moving-sail case. Solution fields at several times. A, $|\mathbf{u}|$ at $t = 5000$ s; B, Pressure at $t = 5000$ s; C, $|\mathbf{u}|$ at $t = 10\,000$ s; D, $|\mathbf{u}|$ at $t = 20\,000$ s; E, $|\mathbf{u}|$ at $t = 40\,000$ s; F, $|\mathbf{u}|$ at $t = 60\,000$ s; G, $|\mathbf{u}|$ at $t = 75\,000$ s; H, $|\mathbf{u}|$ at $t = 90\,000$ s [Colour figure can be viewed at wileyonlinelibrary.com]

6.5 | External and internal fluid flow around a droplet

In this case, an internal circulation pattern developed in a heavier fluid (as water) droplet due to the movement of the surrounding moving lighter fluid (as air) is solved. Analyzing the drop's behavior and its interaction with the environment is important, for example, for spray technology physics, injection in combustion chambers, etc, and its understanding is required to properly model those applications.

The case configuration (geometry, boundary, and initial conditions) is presented in Figure 14. The condition of $\mathbf{u}_n|_{\Gamma_{int}} = 0$ is imposed at the interface, but 2 different cases are solved selecting different values for J. Physical parameters employed are $\rho = 1$, $\mu_1 = 1$, and μ_2 that is variable, and the surface tension is not modeled. Defining $\text{Re} = \frac{\rho|\mathbf{u}|a}{\mu}$, with $a = 0.15$
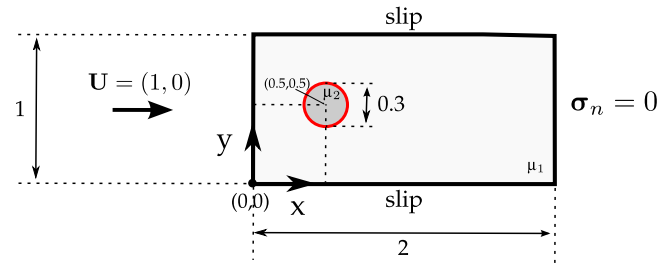
FIGURE 14 Fluid drop case. Geometry and boundary conditions. The red line represents the interface position at $t = 0$, where impenetrability is imposed [Colour figure can be viewed at wileyonlinelibrary.com]
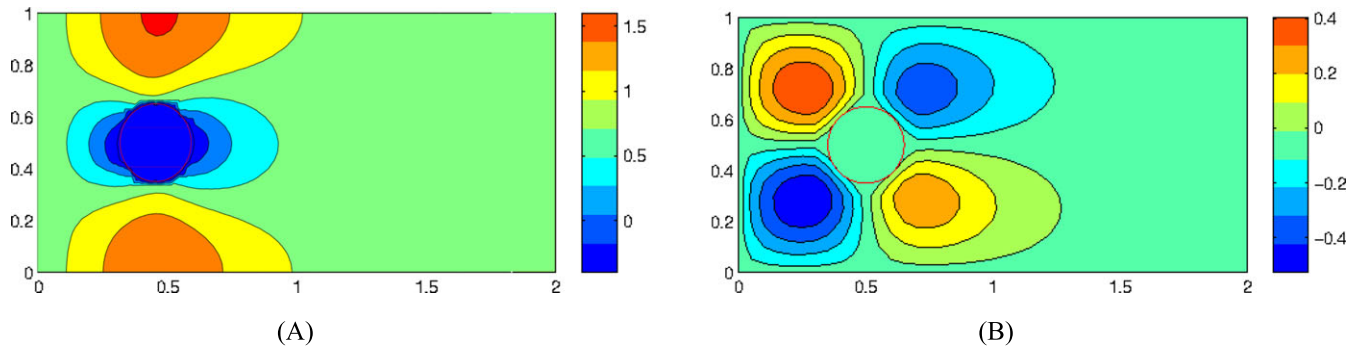

FIGURE 15 Fluid drop case with $J = 0$. A, $\mathbf{u}_x$ and isocontours; B, $\mathbf{u}_y$ and isocontours [Colour figure can be viewed at wileyonlinelibrary.com]
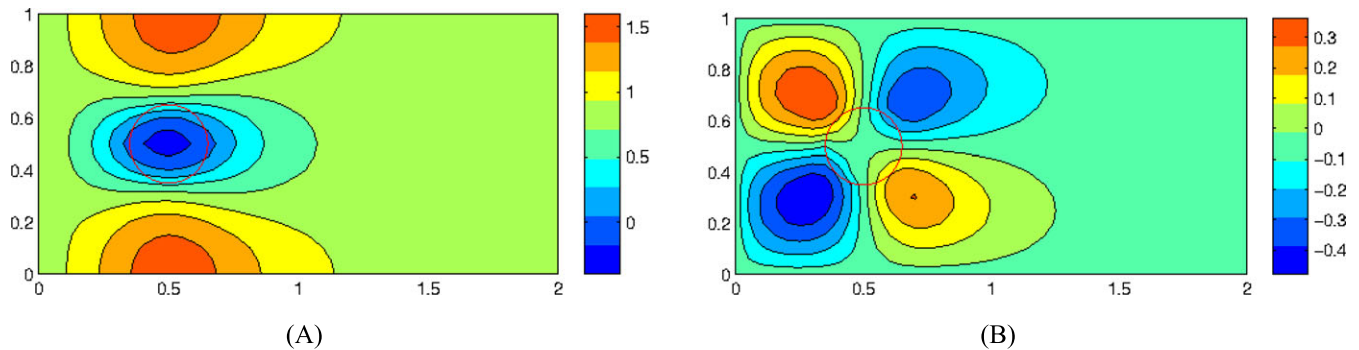

FIGURE 16 Fluid drop case with $J = \infty$. A, $\mathbf{u}_x$ and isocontours; B, $\mathbf{u}_y$ and isocontours [Colour figure can be viewed at wileyonlinelibrary.com]

being the droplet radius, the Reynolds number simulated is Re = 0.15. The mesh employed consists of a Cartesian grid of 60×30 cells split into triangles.

The first case imposes $J = 0$, ie, discontinuity in the tangential velocity at the interface, and $\mu_2 = 0.01$. Its solution should not induce almost any flow inside the drop despite the large viscosity difference. This case is inspired by a fluid flow surrounding a solid sphere or a fluid droplet isolated by a rigid membrane. Figures 15A and 15B show the horizontal and vertical components of the velocity, respectively, for the solution at time $t = 0$. Note that inside the drop, both components vanish, and the exterior flow contours the shape. In Figure 16A, the magnitude of velocity and base mesh employed are shown. It is noticeable how the velocity jump is captured even if the interface cuts an element.

On the other hand, the case with $J = \infty$ and $\mu_2 = 1$ allows a momentum transfer along the interface, inducing a flow inside the drop. The solutions presented in Figures 17 and 16B show that the external fluid motion, in the horizontal direction, results in a doughnut-shaped toroidal flow within the drop known as a Hill's vortex. The cause of the internal circulation is the shear force at the drop surface created by the fluid moving along the surface and allowed by the J selected.

A comparison between the solutions at different J values is presented in Figure 18. The velocity profiles along the horizontal ($x = 0.5$) and vertical ($y = 0.5$) axes are clearly shown as the velocity vanishes inside the drop in the case of
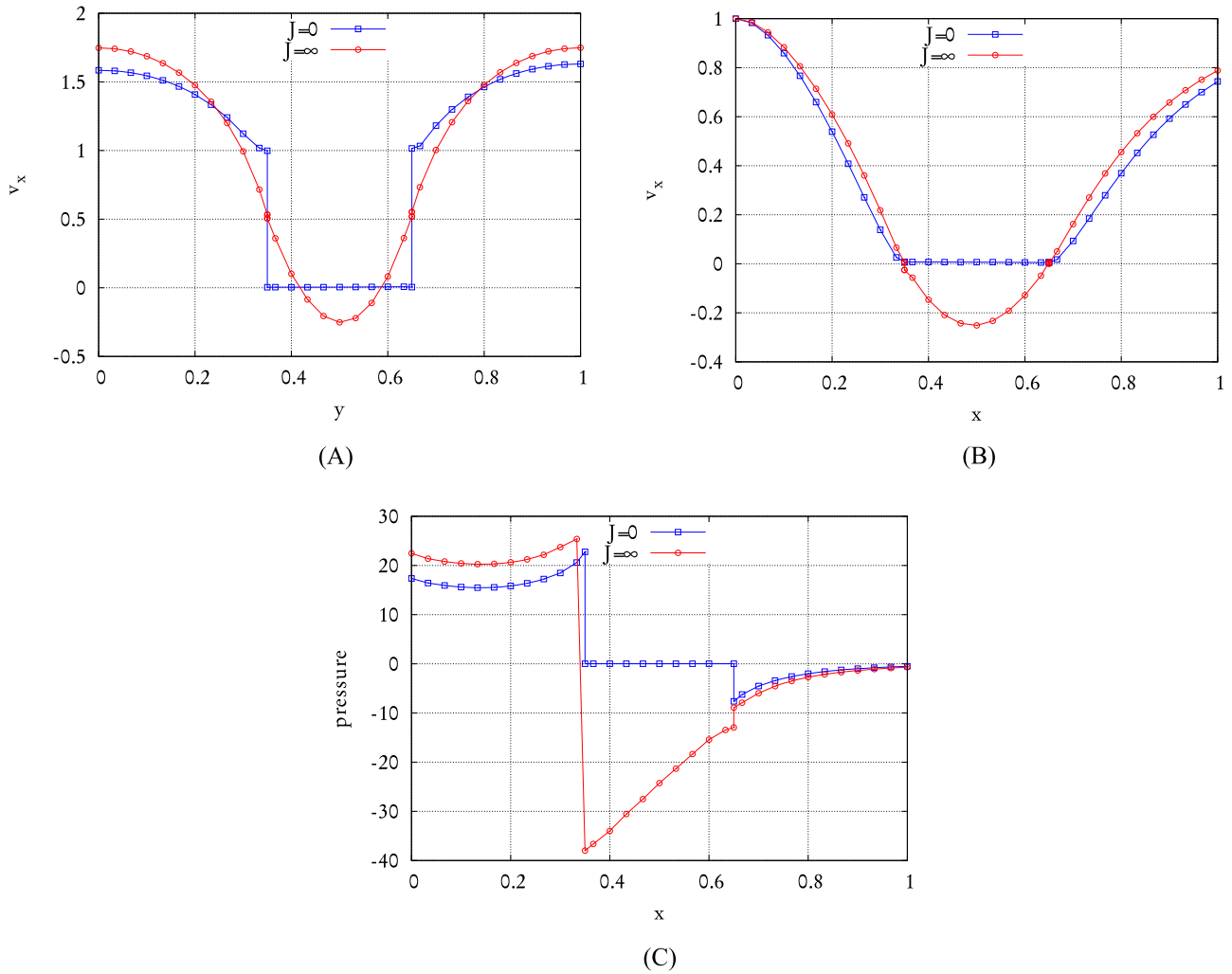
FIGURE 17 Fluid drop case. Profiles of velocity and pressure with different values of J. A, x-velocity along the line $x = 0.5$; B, x-velocity along the line $y = 0.5$; C, Pressure along the line $y = 0.5$ [Colour figure can be viewed at wileyonlinelibrary.com]
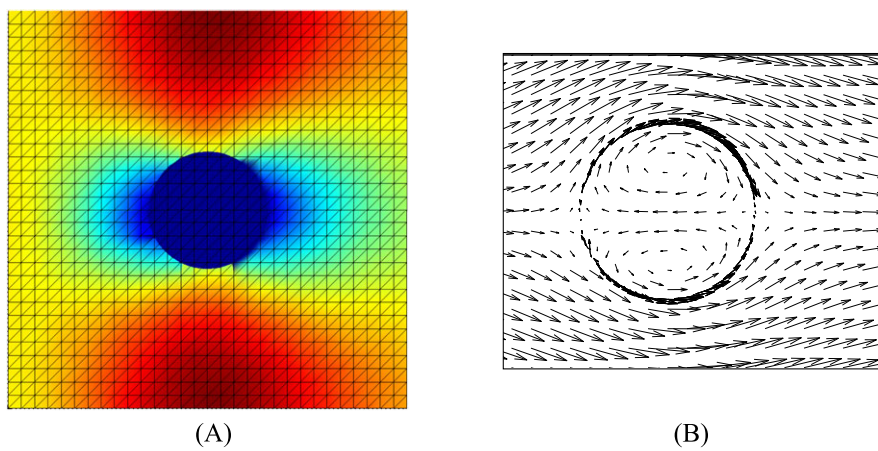

FIGURE 18 Fluid drop case. Velocity fields with different values of J. A, Mesh and $|\mathbf{u}|$. Scale goes from blue to red (0.0-1.6). Case $J = 0$. B, Vectorial representation of the velocity field. Case $J = \infty$ [Colour figure can be viewed at wileyonlinelibrary.com]

$J = 0$. In the solution for $J = \infty$, some checkpoints can be analyzed, which guarantee a physical solution, ie, considering the creeping flow where the velocity magnitude at the interface must be $|\mathbf{u}| = |\mathbf{u}|_{inlet}/2.0$, which is well accomplished by

the solution; this is particularly proven from Figure 18 at the impact point where $\mathbf{u}_x(0.35, 0) = 0$ and at the higher and lower points of the drop, ie, $\mathbf{u}_x(0.5, 0.65) = \mathbf{u}_x(0.5, 0.35) = 0.5$. Both velocity profiles inside the drop describe a parabola with a similar minimum value, showing the presence of the typical pair of vortices induced by an external moving fluid.

The enriched space employed allows also to capture the discontinuity of the pressure field at the interface. In the case of $J = \infty$, the maximum pressure due to the flow impact to the shape occurs in the same numerical point than the minimum inside the drop, while the jump at the other side of the drop is smaller. The captured pressure jump is also noticeable when $J = 0$ is employed. In the latter, the pressure keeps constant to the reference value imposed in one of the droplet nodes ($p = 0$).

7 | CONCLUSIONS

This paper describes how to extend the ideas of using an enriched functional space to capture the discontinuities normally present at interfaces of multifluid flows, either kinks or jumps. After being successfully applied to thermal problems, in this paper, the theory was adapted for a vectorial nonlinear momentum equation constrained by the incompressibility condition as in fluid mechanics. Instead of using a very refined mesh to capture these flow features, this methodology saves a lot of DOFs by using a specially defined functional space that allows for representing in a synthetic way discontinuities in either the function itself or its gradients. Moreover, for problems where the interfaces are constantly moving all around the domain, this strategy based on elemental enrichment (EFEM) may be more adequate than XFEM in terms of efficiency. However, similar to the thermal case, the interelemental loads should be included in order to diminish the variational crime produced by EFEM when using a linear representation along the interface for both the kinks or the jumps. Finally, this new method, to capture the discontinuities at the interface, opens a new horizon in terms of modeling the surface tension and the wall law for turbulence modeling, avoiding a very detailed mesh around the interface.

ORCID

Sergio R. Idelsohn http://orcid.org/0000-0003-0034-7883

REFERENCES

1. Idelsohn SR, Gimenez JM, Marti J, Nigro NM. Elemental enriched spaces for the treatment of weak and strong discontinuous fields. *Comput Methods Appl Mech Eng*. 2017;313:535-559.

2. Unverdi S, Tryggvason G. A front-tracking method for viscous, incompressible, multi-fluid flows. *J Comput Phys*. 1992;100:25-37.

3. Gueyffier D, Lie J, Nadim A, Scardovelli R, Zaleski S. Volume-of-fluid interface tracking with smoothed surface stress methods for three-dimensional flows. *J Comput Phys*. 1999;152:423-456.

4. Popinet S, Zaleski S. A front-tracking algorithm for accurate representation of surface tension. *Int J Numer Methods Fluids*. 1999;30:775-793.

5. Hirt C, Nichols B. Volume of fluid (VOF) method for the dynamics of free boundaries. *J Comput Phys*. 1981;39(1):201-225.

6. Kothe D, Rider W, Mosso S, Brock J, Hochstein J. Volume tracking of interfaces having surface tension in two and three dimensions. Paper presented at: 34th Aerospace Sciences Meeting and Exhibit, Aerospace Sciences Meetings; 1996; Reno, NV. https://doi.org/10.2514/6.1996-859

7. Cummins S, Francois M, Kothe D. Estimating curvature from volume fraction. *Comput Struct*. 2005;83:425-434.

8. Adalsteinsson D, Sethian J. A fast level set method for propagating interfaces. *J Comput Phys*. 1995;118:269-277.

9. Sethian J. Evolution, implementation, and application of level set and fast marching methods for advancing fronts. *J Comput Phys*. 2001;169:503-555.

10. Osher S, Fedkiw R. Level set methods: an overview and some recent results. *J Comput Phys*. 2001;169:463-502.

11. Guermond J, Quartapelle L. A projection FEM for variable density incompressible flows. *J Comput Phys*. 2000;165:167-188.

12. Idelsohn S, Nigro N, Gimenez J, Rossi R, Marti J. A fast and accurate method to solve the incompressible Navier-Stokes equations. *Eng Comput*. 2013;30(2):197-222.

13. Idelsohn S, Marti J, Becker P, Oñate E. Analysis of multifluid flows with large time steps using the particle finite element method. *Int J Numer Methods Fluids*. 2014;75:621-644.

14. Gimenez J, González L. An extended validation of the last generation of particle finite element method for free surface flows. *J Comput Phys*. 2015;284:186-205.

15. Gimenez J. Enlarging time-steps for solving one- and two-phase flows with the Particle Finite Element Method [PhD Thesis]. Santa Fe, Argentina: Facultad de Ingeniería y Ciencias Hídricas (FICH) Centro de Investigacion de Métodos Computacionales (CIMEC) Universidad Nacional del Litoral; 2015.

16. Ganesan S, Matthies G, Tobiska L. On spurious velocities in incompressible flow problems with interfaces. *Comput Meth Appl Mech Eng*. 2007;196:1193-1202.

17. Minev PD, Chen T, Nandakumar K. A finite element technique for multifluid incompressible flow using Eulerian grids. *J Comput Phys*. 2003;187:255-273.

18. Chessa J, Belytschko T. An extended finite element method for two-phase fluids. *J Appl Mech*. 2003;70:10-17.

19. Strouboulis T, Babuška I, Copps K. The design and analysis of the generalized finite element method. *Comput Meth Appl Mech Eng*. 2000;181:43-69.

20. Gross S, Reusken A. An extended pressure finite element space for two-phase incompressible flows with surface tension. *J Comput Phys*. 2007;224:40-58.

21. Barrett JW, Garcke H, Nürnberg H. A stable parametric finite element discretization of two-phase Navier–Stokes flow. *J Sci Comput*. 2015;63:78-117.

22. Oliver J, Huespe A, Samaniego E. A study on finite elements for capturing strong discontinuities. *Int J Num Meth Engrg*. 2003;56:2135-2161.

23. Oliver J, Huespe A, Sánchez P. A comparative study on finite elements for capturing strong discontinuities: E-FEM vs X-FEM. *Comput Methods Appl Mech Engrg*. 2006;195:4732-4752.

24. Ausas R, Buscaglia G, Idelsohn S. A new enrichment space for the treatment of discontinuous pressures in multi-fluid flows. *Int J Numer Methods Fluids*. 2012;70:829-850.

25. Sánchez PJ, Oliver J, Huespe AE, Sonzogni VE. Finite elements with embedded strong discontinuities for the numerical simulation in failure mechanics: E-FEM and X-FEM. In: Larreteguy A, ed. *Mecánica Computacional*. Vol. XXIV. Buenos Aires, Argentina; 2005:541-565.

26. Tezduyar T. Stabilized finite element formulations for incompressible flow computations. *Adv Appl Mech*. 1991;28:1-44.

27. Papanastasiou T, Malamataris N, Ellwood K. A new outflow boundary condition. *Int J Numer Methods Fluids*. 1992;14:587-608.

28. Behr M. On the application of slip boundary conditions on curved boundaries. *Int J Numer Methods Fluids*. 2004;45:43-51.

29. Coppola-Owen H, Codina R. A free surface finite element model for low Froude number mould filling problems on fixed meshes. *Int J Numer Meth Fluids*. 2011;66:833-851.

30. Gimenez J, González L. An extended validation of the last generation of particle finite element method for free surface flows. *J Comput Phys*. 2015;284:186-205.

APPENDIX

In this Appendix, the local assembling of a 2D enriched element and the condensing procedure of the elemental matrix are presented. The ideas showed are easily extensible to the 3D case.

Considering the 2D enriched element presented in Figure A1, the original nodes are tagged as 1, 2, and 3 and the enriched nodes as 4, 5, 6, and 7. Each node has 3 DOFs, namely, u, v, and p for the 2 components of velocity and pressure. Therefore, the elemental assembly of Equation (25) leads to a local equation system with 21 equations and 21 unknowns, ie,

$$
\left[
\begin{array}{ccc|ccc}
\mathbf{K}_{nn}^{uu} & \mathbf{K}_{nn}^{uv} & \mathbf{K}_{nn}^{up} & \mathbf{K}_{ne}^{uu} & \mathbf{K}_{ne}^{uv} & \mathbf{K}_{ne}^{up} \\
\mathbf{K}_{nn}^{vu} & \mathbf{K}_{nn}^{vv} & \mathbf{K}_{nn}^{vp} & \mathbf{K}_{ne}^{vu} & \mathbf{K}_{ne}^{vv} & \mathbf{K}_{ne}^{vp} \\
\mathbf{K}_{nn}^{pu} & \mathbf{K}_{nn}^{pv} & \mathbf{K}_{nn}^{pp} & \mathbf{K}_{ne}^{pu} & \mathbf{K}_{ne}^{pv} & \mathbf{K}_{ne}^{pp} \\
\hline
\mathbf{K}_{en}^{uu} & \mathbf{K}_{en}^{uv} & \mathbf{K}_{en}^{up} & \mathbf{K}_{ee}^{uu} & \mathbf{K}_{ee}^{uv} & \mathbf{K}_{ee}^{up} \\
\mathbf{K}_{en}^{vu} & \mathbf{K}_{en}^{vv} & \mathbf{K}_{en}^{vp} & \mathbf{K}_{ee}^{vu} & \mathbf{K}_{ee}^{vv} & \mathbf{K}_{ee}^{vp} \\
\mathbf{K}_{en}^{pu} & \mathbf{K}_{en}^{pv} & \mathbf{K}_{en}^{pp} & \mathbf{K}_{ee}^{pu} & \mathbf{K}_{ee}^{pv} & \mathbf{K}_{ee}^{pp}
\end{array}
\right]
\left[
\begin{array}{c}
\mathbf{u}_n \\
\mathbf{v}_n \\
\mathbf{p}_n \\
\hline
\mathbf{u}_e \\
\mathbf{v}_e \\
\mathbf{p}_e
\end{array}
\right]
=
\left[
\begin{array}{c}
\mathbf{R}_n^u \\
\mathbf{R}_n^v \\
\mathbf{R}_n^p \\
\hline
\mathbf{R}_e^u \\
\mathbf{R}_e^v \\
\mathbf{R}_e^p
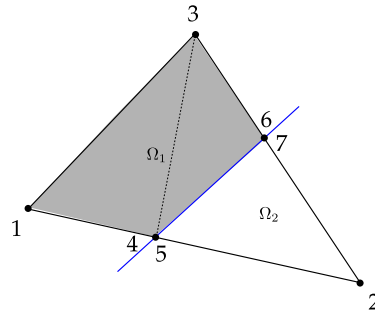\end{array}
\right],
\tag{A1}
$$

FIGURE A1 Enriched element for the 2-dimensional case [Colour figure can be viewed at wileyonlinelibrary.com]

where the subindexes denote the kind of node (original $1 \leq n \leq 3$ or enriched $1 \leq e \leq 4$), and the supraindexes denote the DOF involved. Employing that ordering of the equations, the system can be split, using the lines showed, as

$$
\begin{bmatrix} \mathbf{K}_{nn} & \mathbf{K}_{ne} \\ \mathbf{K}_{en} & \mathbf{K}_{ee} \end{bmatrix} \begin{bmatrix} \boldsymbol{\phi}_n \\ \boldsymbol{\phi}_e \end{bmatrix} = \begin{bmatrix} \mathbf{R}_n \\ \mathbf{R}_e \end{bmatrix},
\tag{A2}
$$

which is condensed in terms of the original nodes as

$$
\left(\mathbf{K}_{nn} - \mathbf{K}_{ne} \mathbf{K}_{ee}^{-1} \mathbf{K}_{en} \right) \boldsymbol{\phi}_n = \mathbf{R}_n - \mathbf{K}_{ne} \mathbf{K}_{ee}^{-1} \mathbf{R}_e.
\tag{A3}
$$